Optics and Lasers in Engineering 195 (2025) 109253

Contents lists available at ScienceDirect

Optics and Lasers in Engineering

journal homepage: www.elsevier.com/locate/optlaseng

KAN-empowered Fano-resonant meta-array coupler for high-sensitivity terahertz detection in HEMTs

Yihao Li [a], Yuxuan Zhai [b], Jiandong Sun [c], Shengji Wang [a], Haoran Wang [d], Xiaojiao Deng [a], Xinhua Li [a], Shijie Wang [e], Chengkuo Lee [f,*], Xiaoping Zheng [a,*]

[a] Department of Automation, Tsinghua University, Beijing 100084, China
[b] Department of Biomedical Engineering, Tsinghua University, Beijing 100084, China
[c] Key Laboratory of Nanodevices and Applications, Suzhou Institute of Nano-tech and Nano-bionics (SINANO), Chinese Academy of Sciences, 398 Ruoshui Road, Suzhou 215123, China
[d] China Academy of Safety Science and Technology, Beijing 100012, China
[e] Department of Biomedical Engineering, National University of Singapore, 117583, Singapore
[f] Department of Electrical and Computer Engineering, National University of Singapore, 117583, Singapore

ARTICLE INFO

Keywords:
GaN HEMT
Deep learning
Metasurface
Detector
Fano resonant

ABSTRACT

On-chip couplers play a critical role in converting high-frequency terahertz (THz) radiation into detectable near-field signals, fundamentally determining the sensitivity of high-electron-mobility transistor (HEMT)-based THz detectors. Conventional single-unit HEMT detectors employing standard antenna designs face inherent limitations: they must compromise between achieving high resonance intensity and maintaining broad bandwidth coverage. To address this fundamental trade-off, we present a highly efficient meta-array coupler that leverages Fano resonance, complemented by a dedicated deep-learning design framework utilizing Kolmogorov-Arnold Networks (KAN). Our meta-array architecture demonstrates remarkable performance improvements over conventional bow-tie couplers, expanding the operational bandwidth from 270 GHz to 972 GHz—a 3.6-fold enhancement. Crucially, the Fano resonance arising from the integration of split-ring resonators (SRR) with bow-tie antennas in our meta-coupler design achieves a dramatic 70-fold enhancement in the antenna factor at the resonance frequency, delivering near-field coupling efficiencies that fundamentally surpass the capabilities of standalone antenna structures. The versatility of our proposed structure and predictive framework extends beyond this specific implementation, offering a generalizable approach for customized meta-array designs tailored to specific frequency requirements. This advancement significantly reduces the performance gap between current THz detector capabilities and the demanding requirements of next-generation THz applications.

1. Introduction

Terahertz (THz) radiation, occupying the spectral region between infrared and microwave frequencies, has gained significant attention for biomedical imaging [1], chemical sensing [2,3], high-speed communication [4–6] and non-destructive diagnostics [7,8] due to its unique low photon energy and molecular fingerprinting capabilities [9–11]. Unlike infrared radiation, THz waves exhibit millielectronvolt-level photon energy, enabling non-ionizing interactions with biological tissues while penetrating non-polar materials—a critical advantage for in vivo imaging. However, practical applications face two fundamental limitations: the inherently low output power of existing solid-state THz frequency multipliers [12] and severe signal attenuation caused by the high water content of biological tissues [13], which collectively hinder the detection of weak THz signals.

High-electron-mobility transistor (HEMT)-based detectors have emerged as promising candidates for room-temperature THz detection, offering high-speed operation and CMOS compatibility [14–18]. Yet their performance is constrained by a critical dimensional mismatch: the microscale HEMT channel dimensions are orders of magnitude smaller than the submillimeter THz wavelengths. This mismatch necessitates on-chip couplers to enhance near-field coupling efficiency [19]. Conventional dipole couplers suffer from low quality factors and weak resonant strengths, failing to generate sufficient self-mixing electric

* Corresponding authors.
E-mail addresses: elec@nus.edu.sg (C. Lee), asean@mail.tsinghua.edu.cn (X. Zheng).

https://doi.org/10.1016/j.optlaseng.2025.109253
Received 26 June 2025; Received in revised form 27 July 2025; Accepted 2 August 2025
Available online 8 August 2025

fields in the gated channel for high-sensitivity detection [20–22]. While advanced subwavelength structures—including three-lobed dipoles [20], bowtie antennas [23], and periodic gratings [24]—have improved localized field enhancement, their performance remains limited by inherent trade-offs between bandwidth and intensity in single-resonance systems. Recent advances in impedance-matching optimization have demonstrated progress in THz detection sensitivity. Bauer et al. achieved a noise-equivalent power (NEP) of 31 $\mathrm{pW}/\sqrt{\mathrm{Hz}}$ at 600 GHz through systematic detector impedance tuning [25]. While such strategies—including coplanar waveguides and metamaterial-loaded gate configurations [24] —enhance energy transfer efficiency, they remain insufficient for addressing the fundamental limitation of weak field amplification within the HEMT channel.

Recent advances in Fano resonance systems, leveraging discrete-continuum state interference effects, have demonstrated unprecedented spectral control in nanophotonics and plasmonics [26,27]. Asymmetric meta-atom arrays enable synergistic optimization of narrowband high-Q resonances and broadband responses [28,29], offering new possibilities for overcoming HEMT field enhancement limits. However, the extreme geometric sensitivity of Fano resonators to structural parameters like inter-element spacing makes traditional trial-and-error design approaches prohibitively time-consuming and costly. Although deep learning has shown promise in metasurface modeling, no specialized neural network frameworks exist for Fano coupler design in HEMT detectors.

This study introduces a Fano-resonant meta-array coupler that synergistically combines a strongly resonant split-ring structure with a broadband bowtie antenna to generate intense localized electric fields beneath the HEMT gate. The results demonstrate a 270–972 GHz operational bandwidth ($\Delta f = 702$ GHz), representing a huge improvement over conventional bowtie couplers, with a 70-fold antenna factor enhancement at the Fano resonance peak. Furthermore, we present a Kolmogorov-Arnold Network (KAN)-based forward design framework—the first application of deep learning for HEMT coupler resonance prediction and structural optimization. By leveraging KAN's theorem-driven univariate decomposition and parameter-efficient architecture, we achieve rapid, accurate modeling of subwavelength array electromagnetic responses. This integrated approach of meta-array engineering and neural network-driven design provides a systematic pathway for developing high-performance THz detection systems.

2. Design and method

Based on the antenna-coupled HEMT self-mixing model with passive drain bias [19], the self-mixing photocurrent generated in the transistor can be represented as

$$\begin{cases} i_0 \propto P_0 Z_0 \overline{z} \Xi(V_g) \Lambda_0(\omega) \\ \Lambda_0(\omega) = \int_0^L \dot{\xi}_x \dot{\xi}_z \cos\phi \mathrm{d}x \\ \Xi(V_g) = \mathrm{d}G/\mathrm{d}V_g \end{cases} \tag{1}$$

Where $P_0(\omega)$is the received THz energy flux, $Z_0 = 377\ \Omega$ is the free-space impedance,$\overline{z}$ is the effective distance between the gate and the channel, respectively. Field-effect factor $\Xi(V_g)$ characterizes the gate voltage's ability to modulate the channel conductance G,which is determined by the quantum well structure and the Schottky gate. The most critical and important antenna factor $\Lambda_0(\omega) = \int_0^L \dot{\xi}_x \dot{\xi}_z \cos\phi \mathrm{d}x$ is the integral of the mixing factor $M(x) = \dot{\xi}_x \dot{\xi}_z \cos\phi$ within the gated two-dimensional electron gas (2DEG) channel, which is determined by the detector's ability to couple with the THz field. $\dot{\xi}_x = E_x/E_0$, $\dot{\xi}_z = E_z/E_0$, and ϕ represent the horizontal and vertical THz field enhancement factors within the gated 2DEG channel and the phase difference between the induced fields, respectively.

Currently, the primary limiting factor for achieving higher sensitivity in HEMT-based THz detectors, aside from transistor transconductance, is the excitation efficiency described by the antenna factor. Enhancing near-field coupling over a broad frequency band places multiple, often conflicting, requirements on the design of on-chip couplers. However, conventional antenna structures struggle with significant dimensional mismatches, limiting their ability to enhance the self-mixing electric fields effectively within the transistor's gate-controlled channel.

To address these challenges of achieving strong near-field coupling and rapidly designing complex parameter structures, we propose a synergistic hardware-software solution that integrates advanced on-chip coupler design with deep learning-based prediction. Specifically, we developed a meta-array coupler capable of Fano resonance by integrating strongly resonant split-ring resonators (SRRs) with weakly resonant broadband bowtie structures, substantially enhancing near-field coupling. Complementing this hardware approach, we introduce a KAN-based deep learning model trained specifically for rapid prediction of resonance spectra, enabling efficient optimization through nonlinear mapping between coupler geometry and near-field enhancement characteristics.

The meta-array structure is shown in Fig. 1(a), and an enlarged view of its unit cell is presented in Fig. 1(b). It is designed on a standard thinned GaN heterostructure substrate with dimensions of $360 \times 360\ \mu$m. The metallic components, composed entirely of gold due to its high conductivity and low loss at THz frequencies, include critical parameters such as the gap and radius (R_o) of the ring-shaped SRR, as well as the bowtie length parameter (L_a) with an opening angle of 60° The AlGaN layer has a dielectric constant of 8.9 and a thickness of 23 nm. Therefore, particular attention is given to the field enhancement at the 23 nm depth beneath the meta-array, where the self-mixing channel is located. To accurately reflect realistic device conditions, the source and drain electrodes were also included in simulations.

The meta-array's complex structure and multiple design parameters make full-wave simulations computationally expensive, posing challenges for customizing the resonant frequency. To address this, we introduce a deep neural network based on KAN for the first time in terahertz detection, as shown in Fig. 1(c-d). This network establishes a complex nonlinear mapping between design parameters and the resonant spectrum. Unlike traditional MLPs, KANs apply learnable activation functions to weights rather than neurons, allowing for greater flexibility in processing input data and more accurate modeling of intricate variable relationships. All training data were generated through finite element method (FEM) simulations, with a perfectly matched layer (PML) boundary condition applied along the z-direction to minimize reflections. The incident terahertz wave propagates along the $-z$ direction with linear polarization along the x-axis. To quantify the mixing factor and antenna factor in Eq. (1), we focused on extracting the transverse (E_x) and longitudinal (E_z) enhanced electric fields at a depth of 23 nm beneath the grating. This extensive dataset serves as the foundation for training the deep neural network and evaluating the meta-array's performance.

3. Results and discussion

3.1. Field enhancement characteristics of SRR in the gated channel

To gain a deeper understanding of the meta-array's resonant properties, we first examined the near-field coupling at a depth of 23 nm beneath the gate for an isolated SRR. As shown in Fig. 2(a), the SRR structure is characterized by two key parameters: the *gap* and the outer ring radius R_o. When a THz field is applied to the nanogap, it induces a strong local electric field enhancement, resulting in an effective carrier multiplication effect. This intensified local field interacts with the substrate, increasing the nonlinearity of its local conductivity and making the SRR functionally analogous to a closed-ring resonator (CRR) [30].

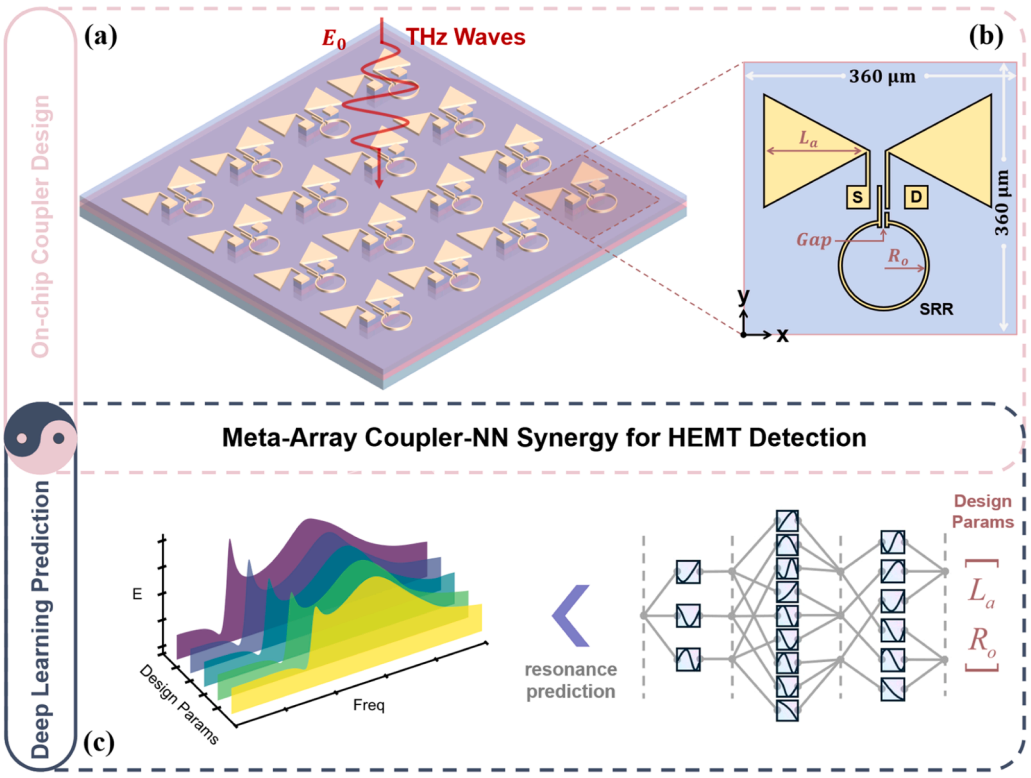

Fig. 1. Synergistic integration of meta-array coupler and neural network for HEMT Detection. (a) Schematic of the meta-array structure. (b) Schematic of the meta-atom structure with a period of 360 × 360μm. (c) A KAN-based deep neural network models the nonlinear relationship between design parameters and the near-field coupling electric field of the meta-array.

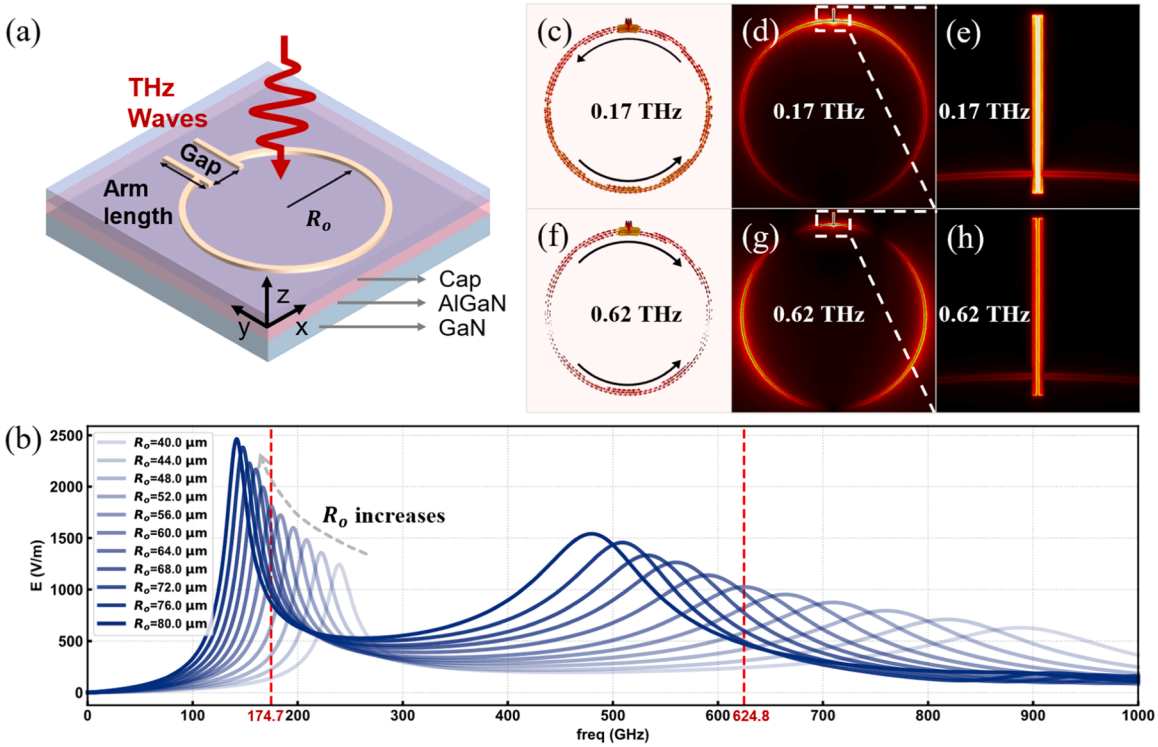

Fig. 2. Structure of the split ring resonator and related performance characterization. (a) 3D schematic of the proposed SRR structure and its related geometric dimensions. (b) The curve of electric field intensity as a function of the frequency of the incident electromagnetic wave, measured at the center of the gap, 23 nm below the surface of the substrate, when the gap is 0.15 μm. When the radius R_o = 60 μm, two enhancement points can be observed at 174.7 GHz and 624.8 GHz, respectively, marked with red dashed lines. (c) and (f) respectively illustrate the surface current distribution of the SRR at the 174.7 GHz and 624.8 GHz points indicated by the dashed lines in (b). The black arrows denote the directions of surface electric current. (d) and (g) display the electric field energy density distribution at the corresponding frequencies. The magnified view near the gap is shown in (e) and (h).

When the gap size is 0.15 μm, the electric field enhancement curves at a depth of 23 nm within the substrate at the center of the gap for different R_o are shown in Fig. 2(b). It is evident that the single SRR structure leads to two resonance peaks. As the radius R_o increases, the resonance peak of the SRR at that point gradually shifts towards lower frequencies. Simultaneously, the localized electric field strength excited at this location is significantly enhanced with the increase of R_o, indicating an inverse relationship with the radius.

The resonance mechanism of the isolated SRR was analyzed by examining the two resonance peaks marked by red dashed lines in Fig. 2 (b). When $R_o = 60$ μm, two distinct resonance modes appear at $f_1 =$ 174.7GHz and $f_2 = 624.8$ GHz. To better understand the underlying physical mechanisms, numerical simulations were conducted to examine the surface currents and electric energy densities at these resonance frequencies. Fig. 2(c)–(e) depict the surface current, electric field intensity distribution, and local electric field enhancement at the gap for the f_1 resonance, respectively, while Fig. 2(f)–(h) show the corresponding distributions for f_2. The two resonance modes exhibit distinct surface current patterns: at f_1, the current circulates counter-clockwise around the entire ring, whereas at f_2, the surface current splits and flows in opposite directions. This strongly indicates that the low-frequency resonance corresponds to a magnetic dipole response, while the high-frequency resonance arises from an electric dipole mode. Achieving high Q-factor resonance in the gap for both dipole responses can enhance the coupling of THz fields in traditional GaN HEMT THz detectors. Due to the significant impedance mismatch, only a small fraction of the THz power is coupled into the mixing region [31]. The locally enhanced electric field can substantially mitigate this issue. Therefore, we specifically focus on the electric field distribution at the center of the gap, 23 nm below the substrate surface, as this region is crucial for the self-mixing operation of the field-effect detector. This focus distinguishes our work from other SRR-related studies [32,33]. Fig. 2(e-h) show that the electric field distribution at both resonance points is significantly concentrated in the gap, demonstrating substantial enhancement compared to the substrate without structures. Quantitative analysis of the extracted electric field reveals that the enhancement factor β is approximately 1811 at 174.7 GHz, relative to the substrate without the SRR structure. Even at non-resonant frequencies, the field enhancement factor remains two orders of magnitude higher. The local high Q-factor characteristic effectively addresses the poor coupling capability of GaN HEMT THz detectors to the local mixing region's electric field due to impedance mismatch issues [19].

Therefore, particular emphasis is placed on the meta-structure's capability to enhance the coupled electric field in the gated channel. $\dot{\xi}_{x_{SRR}} = E_x/E_0$ and $\dot{\xi}_{z_{SRR}} = E_z/E_0$ were defined to characterize the meta-atom's influence on the mixing factor. As previously discussed, variations in the SRR radius R_o inversely affect the resonance frequency, while changes in the SRR's structural dimensions significantly impact the enhancement factors $\dot{\xi}_{x_{SRR}}$ and $\dot{\xi}_{z_{SRR}}$. Fig. 3 illustrates the effect of the gap and R_o dimensions of the meta-atom on $\dot{\xi}_{x_{SRR}}$. Fig. 3(a), 2(b), and 3 (c) show the impact of different gap sizes on $\dot{\xi}_{x_{SRR}}$ for $R_o = 40$ μm, 60 μm and 80 μm, respectively. Fig. 3(d), 3(e), and 3(f) depict the influence of different R_o values on normalized $\dot{\xi}_{x_{SRR}}$ for gap sizes of 0.15 μm, 0.25 μm, and 0.35 μm, respectively. With a consistent R_o, the magnitude of $\dot{\xi}_{x_{SRR}}$ at the resonance frequency is inversely proportional to the gap size. Additionally, as the gap increases, the resonance frequency slightly increases. According to the formula $E_{gap} = V_{gap}/\text{gap}$, for a constant R_o, the area exposed to the THz field remains nearly unchanged. Thus, with nearly constant induced voltage, a smaller gap results in a higher local electric field intensity. For the same gap, the effect of different R_o on normalized $\dot{\xi}_{x_{SRR}}$ is consistent with Fig. 3(b). As R_o increases, the peak frequency significantly decreases, corresponding to the SRR's magnetic and electric dipole modes.

Adjusting the two key parameters, R_o and the gap, tunes the enhancement frequency point and the mixing factor's enhancement factor. This capability allows for the unique customization of meta-atoms for desired frequency bands in the THz Meta-Coupler. Fig. 4(a) summarizes the effect of the meta-atom radius R_o on the distribution of $\dot{\xi}_{z_{SRR}}$ with a 0.15 μm gap. As R_o increases from 40 μm to 80 μm, the resonance peaks of both observed modes shift towards lower frequencies linearly, accompanied by an increased enhancement factor and broader FWHM, indicating better coupling with the incident THz field. This

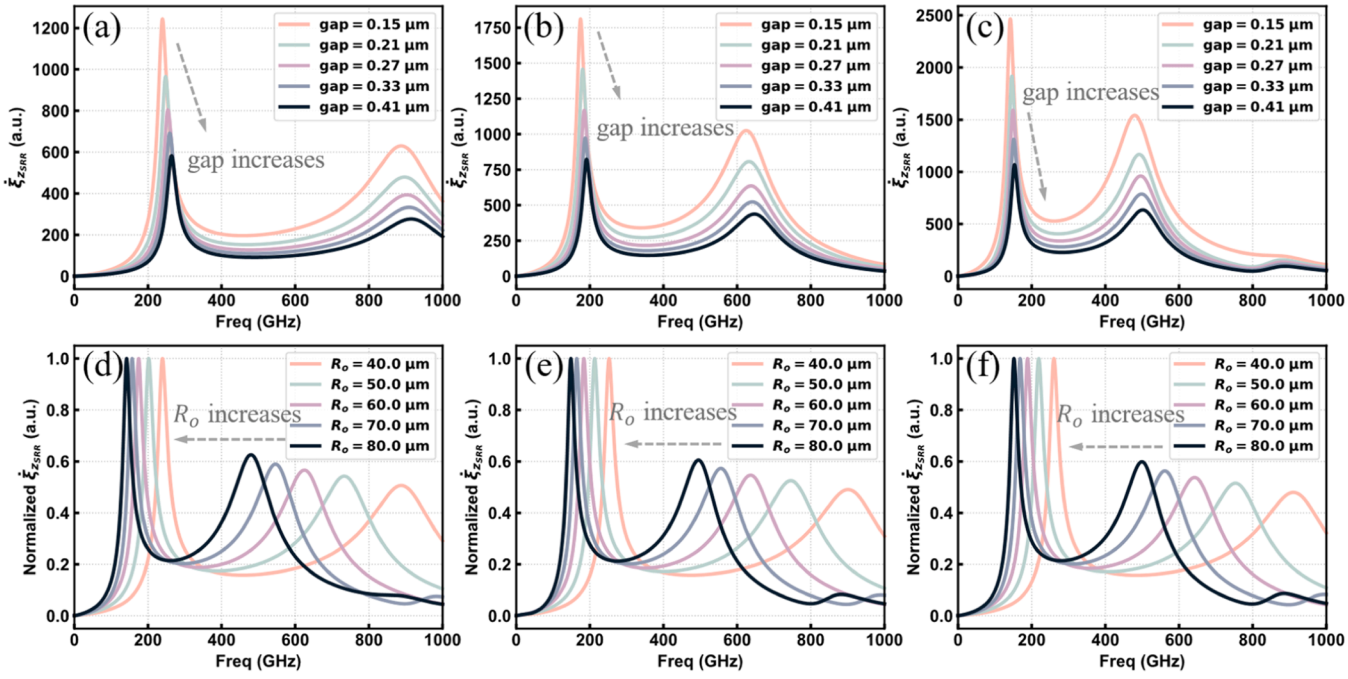

Fig. 3. Illustrates the impact of R_o and gap variations on the localized field enhancement of the SRR. Each subfigure presents the electric field intensity at a fixed location, specifically at the center of the gap, 23 nm within the dielectric. (a), (b), and (c) correspond to SRRs with R_o values of 40 μm, 60 μm, and 80 μm, respectively. (d), (e), and (f) correspond to SRRs with gap size of 0.15 μm, 0.25 μm, and 0.35 μm.

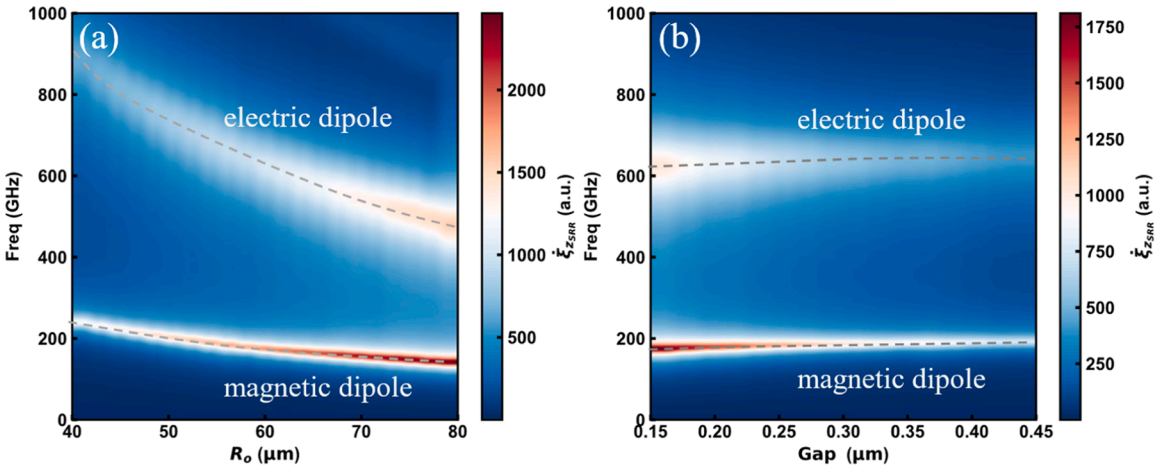

Fig. 4. Illustrates the relationship between the SRR's gap, radius R_o, and resonance intensity below 1000 GHz. The gray dashed lines mark the frequencies of the two peak resonance enhancements. (a) THz field enhancement at the point of interest (23 nm within the central substrate) as a function of R_o with a 0.15 μm gap. (b) THz field enhancement at the same point as a function of the gap, with R_o fixed at 60 μm.

enhances the self-mixing efficiency of field-effect detectors. Conversely, the gap mainly affects the Q-factor of the resonance, as shown in Fig. 4 (b). With R_o set to 60 μm, as the gap decreases from 0.45 μm to 0.15 μm, the gray dashed line remains nearly constant, but the Q-factor significantly increases. This indicates that optimizing the gap size within semiconductor manufacturing limitations can substantially enhance the enhancement factor $\dot{\xi}_{z_{SRR}}$ at the desired point. The ability to flexibly select R_o and the gap enables customization of detectors to target specific frequency points, addressing a major limitation of traditional architectures. This represents a significant advancement in detector design.

3.2. Meta-array architecture and the generation of Fano resonance

Fig. 5(a) presents a schematic diagram of the proposed Meta-Coupler. Fig. 5(b) illustrates the schematic diagram of a common field-effect detector architecture (hereafter referred to as Con-Coupler, widely adopted in many studies [25]. Since the substrate and gate of the transistor are identical in both devices, the ideal mixing factor $\Xi(V_g)$ remains the same. The only difference lies in the surface coupler. Therefore, the key factor affecting the detection performance of GaN HEMTs with the same specifications is the antenna factor $\Lambda_0(\omega)$ [19]. Due to their different coupling architectures, and based on the analysis of the Meta-Coupler enhancement factor in Section 2. The transverse and longitudinal enhancement factors for this architecture can be decomposed into contributions from both the meta-atom and the coupling antenna, where $\dot{\xi}_{x_{Metadet}}$ consists of the contribution from $\dot{\xi}_{x_{SRR}}$ of the SRR and $\dot{\xi}_{x_{an}}$ of the antenna, and similarly for $\dot{\xi}_{z_{Metadet}}$. In contrast, for the Con-Coupler architecture, the enhancement factors arise solely from the coupling antenna, given by $\dot{\xi}_{x_{Det}} = \dot{\xi}_{x_{ant}}$ and $\dot{\xi}_{z_{Det}} = \dot{\xi}_{z_{ant}}$.

According to the self-mixing model, mixing is highly localized within the gate-controlled 2DEG channel. Consequently, the electric field strength 23 nm below the center of the gate, referred to as the point of interest, is a crucial parameter for evaluating the performance of the field-effect detector. Fig. 6(d) illustrates the relationship between electric field intensity and incident frequency at points of interest for the coupler of conventional detector with L_a = 100, 120, and 140 μm. The curve exhibits a symmetric quasi-Lorentzian lineshape within the 0–1000 GHz range. The detector, integrated with bowtie antennas of varying lengths, shows an optimal operating point within this frequency band. For L_a = 140 μm, the optimal frequency f_{Con1} is 476 GHz with a peak intensity of 668 V/m; for L_a = 120 μm, f_{Con2} is 537 GHz with a peak intensity of 551 V/m; and for L_a = 100 μm, f_{Con3} is 641 GHz with a peak intensity of 461 V/m. The antenna length L_a is inversely proportional to the center frequency f_{Con}, following a relationship similar to that of a dipole antenna, $f_0 \sim c/(4\sqrt{\bar{\epsilon}}L_A)$, where L_a is the antenna length shown in the Fig. 5. c is the speed of light in a vacuum, and $\bar{\epsilon} \approx (1+\epsilon)/2$ [16].As the antenna size decreases, the field strength induced at the point of interest by the coupling antenna in response to the same incident plane wave E_0 gradually decreases. However, the optimal operating frequency f_{Con} increases, accommodating higher frequency detection requirements. This highlights the trade-off problem faced by

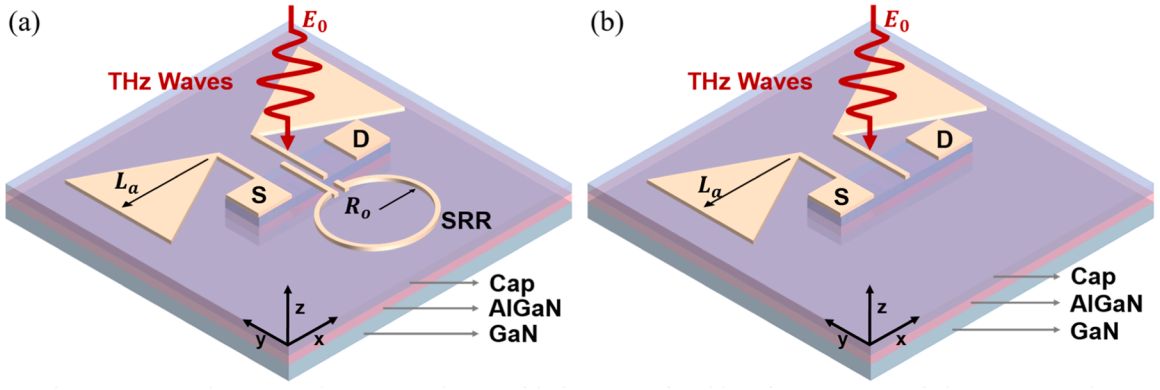

Fig. 5. Compares the proposed Meta-Coupler (a) with the conventional bowtie antenna-coupled GaN HEMT detector (b). In the conventional design, a bowtie antenna (arm length L_a, flare angle $\theta = 60^\circ$) is integrated onto the HEMT's source and gate, enabling detection of x-polarized terahertz waves.

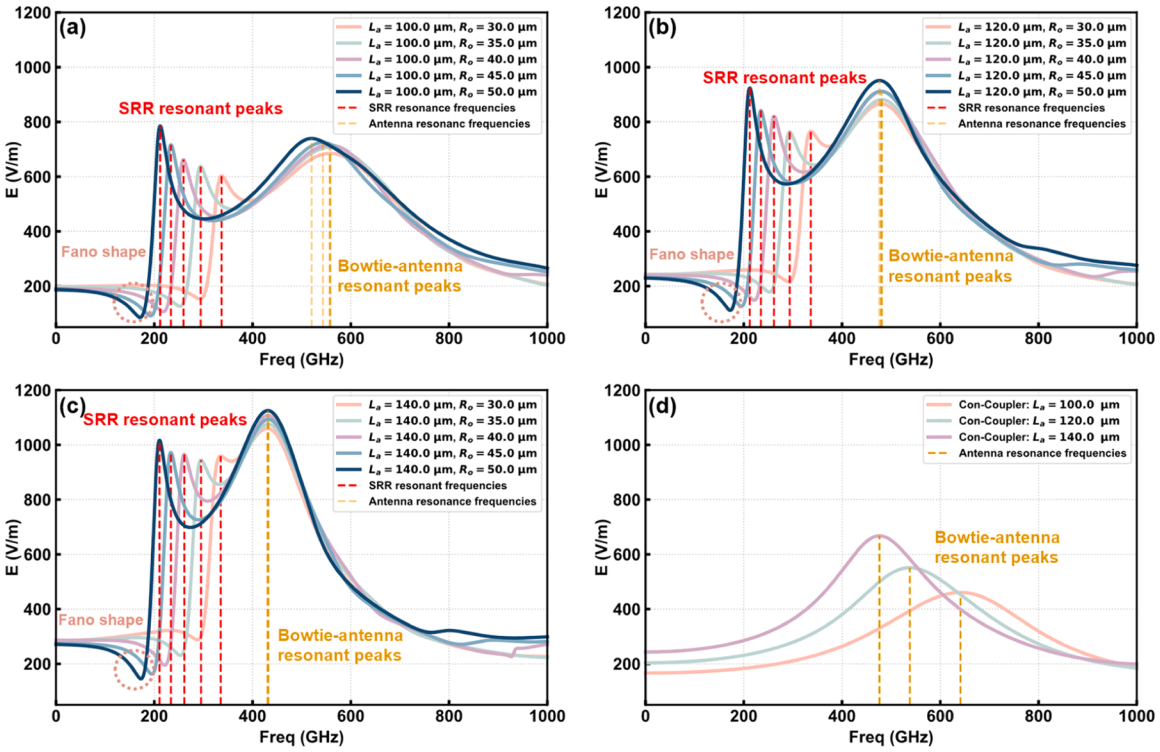

Fig. 6. Comparison of electric field intensity in the 23 nm channel beneath the gate for Meta-Coupler with various L_a and R_o values as the incident terahertz wave frequency changes, with a gap of 0.15 μm. (a) (b) (c) show the impact of different R_o values on the local electric field under the gate of the Meta-Coupler for L_a = 100, 120, and 140 μm. (d) illustrates the relationship between the incident frequency and the electric field intensity at the same position under the gate of conventional GaN HEMT terahertz detectors with L_a = 100, 120, and 140 μm. The yellow dashed lines indicate the position of the resonance peak introduced by the bowtie antenna, while the red dashed lines show the positions of the additional resonance peaks introduced by SRRs with various R_o sizes.

conventional field-effect detectors: balancing induced field strength with the optimal frequency f_{Con}. Typical bowtie and dipole antenna-coupled field-effect detectors face difficulties in overcoming this issue [16].

To investigate the differences in electric field coupling modes between the proposed Meta-Coupler architecture and traditional detectors, the same coupling antenna length L_a was used for both detection chips to minimize its influence on electric field intensity distribution in the gated channel region. Fig. 6(a), (b), and (c) show the relationship between electric field strength and incident THz wave frequency for Meta-Coupler with L_a = 100, 120, 140 μm and R_o = 30, 35, 40, 45, 50 μm. Each subplot shows two resonance peaks: f_1 (related to the meta-atom structure) and f_2 (determined by the coupled antenna). As the meta-atom radius increases, the f_1 resonance peak frequency decreases, and the coupled electric field strength increases, as observed in Meta-Coupler with L_a = 100, 120, 140 μm. This behavior resembles the SRR unit study but with differences. The red dashed circle shows a Fano shape, contrasting with the symmetric quasi-Lorentzian lineshape in Fig. 3 The physics of Fano resonances can be explained using a model of two coupled driven oscillators, described by the following matrix equation [34,35,27]:

$$\begin{pmatrix} \omega_1 - \omega - i\gamma_1 & g \\ g & \omega_2 - \omega - i\gamma_2 \end{pmatrix} \begin{pmatrix} x_1 \\ x_2 \end{pmatrix} = i \begin{pmatrix} f_1 \\ f_2 \end{pmatrix} \tag{2}$$

Here, γ_1 and γ_2 are the damping coefficients, x_1 and x_2 represent the oscillator amplitudes, ω_1 and ω_2 are the resonant frequencies, and f_1 and f_2 are the external forces with the driving frequency ω. The coupling constant g characterizes the interaction between the oscillators. Fano resonance arises from the coupling of two oscillators with significantly different damping rates, resulting in narrow and broad spectral lines. The coupling constant g is smaller than the larger damping coefficient γ. In the Meta-Coupler architecture, both the strong resonance generated by the SRR and the relatively mild resonance from the coupled antenna are introduced simultaneously. The coupling of these two oscillators with significantly different damping rates results in the Fano resonance depicted by the red dashed lines in Fig. 6 The amplitude of the driven oscillator 1 (meta-atom) near the resonance frequency of oscillator 2 (bow-tie antenna) can be expressed as [27]: $|x_1(\Omega)|^2 \approx |f_1^2| \frac{{\gamma_1}^2}{(\omega_1-\omega_2)^2+{\gamma_1}^2} \frac{(\Omega+q)^2}{(\Omega^2+1)}$. Where $\Omega = \left[\omega - \omega_2 + \left(\frac{g^2}{\gamma_1}\right)\frac{(\omega_1-\omega_2)}{1+q^2}\right]\frac{\gamma_1(1+q^2)}{g^2}$ is the dimensionless frequency. The Fano parameter q determines the spectral shape and depends on the spectral detuning between the oscillators $\omega_2 - \omega_1$. By comparing the electric field values in Fig. 3 and Fig. 6(d), we found that the coupling-induced Fano resonance further enhances the original resonances of the SRR and bowtie antenna, thereby strengthening the coupling capability of the Meta-Coupler architecture to the terahertz field. To our knowledge, this is the first observation of Fano resonance enhancement in the gate-controlled channel of a HEMT-based terahertz detector. The introduction of this new resonance mechanism offers a novel design concept and theoretical foundation for optimizing and developing the next generation of field-effect detectors.

To gain deeper insight into the coupling interactions between the SRR and the bowtie antenna, we employed coupled-mode theory (CMT) to analyze the spectral response characteristics of the different structures. Based on the distinct coupling mechanisms, three analytical lineshape models were established: (i) a single Lorentzian model (Eq. (1)) to describe the resonance behavior of an isolated antenna, (ii) a double Lorentzian model (Eq. (2)) to characterize an isolated SRR exhibiting two resonant modes, and (iii) a double Fano model (Eq. (3)) to capture the spectral features of the coupled Meta-Coupler. In these models, the Fano asymmetry factor (q) is defined using the normalized frequency parameter and is extracted from the experimental spectra via a least-squares fitting procedure. The definitions of the quality factor (Q) and

the damping factor (γ) used in the models are provided as Eq. (6), Eq. (7).

$$I(\omega) = I_{bg} + A\frac{\gamma^2}{(\omega-\omega_0)^2+\gamma^2} \tag{3}$$

$$I(\omega) = I_{bg1} + A_1\frac{\gamma_1^2}{(\omega-\omega_{01})^2+\gamma_1^2} + I_{bg2} + A_2\frac{\gamma_2^2}{(\omega-\omega_{02})^2+\gamma_2^2} \tag{4}$$

$$I(\omega) = I_{bg1} + A_1\frac{(q_1+\varepsilon_1)^2}{1+\varepsilon_1^2} + I_{bg2} + A_2\frac{(q_2+\varepsilon_2)^2}{1+\varepsilon_2^2} \tag{5}$$

$$Q = \frac{f_0}{\mathrm{FWHM}} \tag{6}$$

$$\gamma = \frac{\omega_0}{2Q} \tag{7}$$

As shown in Fig. 7, we conducted a systematic spectral fitting analysis for the three devices: the antenna (L_a = 100 μm), the SRR (r_o = 40 μm), and the metasurface coupler (L_a = 100 ,r_o = 40 μm). The coefficients of determination (R^2) of the fitted results reached 0.939, 0.998, and 0.999, respectively, confirming the high accuracy and reliability of the proposed models. Notably, the double-Fano fitting for the Meta-Coupler achieved an R^2 as high as 0.999, clearly demonstrating that the integrated structure supports a high-purity Fano resonance. From the fitted parameters, we successfully extracted the damping rate (γ), quality factor (Q), and Fano asymmetry parameter (q) for each resonant mode. The corresponding values are summarized in Table 1. The meta-coupler that generates Fano resonances exhibits higher Q factors in both modes compared with the SRR and the antenna. This superior performance indicates that the meta-coupler has great potential for enhancing molecular fingerprint sensing applications [36].

Furthermore, analysis of the resonance frequencies enables us to unambiguously identify the origins of the two Fano modes: Fano mode 1 (633 GHz) arises from the coupling between SRR mode 1 and the antenna, whereas Fano mode 2 (565.5 GHz) results from the interaction between SRR mode 2 and the antenna.

All f values in the table are in GHz, E values are in V /m, and L_a and R_o values are in μm.

To illustrate the resonances in the Meta-Coupler and compare them with the Con-Coupler, Table 2 shows the bowtie antenna resonant peaks (f_{Con1}) from the 3 Con-Coupler in Fig. 6, alongside the meta-atoms (f_1) and bowtie antenna (f_2) peaks from the 15 Meta-Couplers. For Meta-Couplers with the same R_o, f_1 values vary by only 1–2 GHz, indicating that L_a length has minimal impact on f_1. This supports the conclusion that the f_1 resonant point is primarily determined by the meta-atom. For Meta-Coupler with the same L_a size, the f_2 resonance remains nearly unchanged despite different meta-atom R_o sizes. This indicates that R_o variations minimally impact the f_2 peak, which is primarily determined by the bowtie antenna. Additionally, the electric field intensity at the Meta-Coupler's resonant peaks is significantly higher than that of the Con-Coupler with the same L_a. When L_a = 140 μm, the field strength at f_1 of the Meta-Coupler (R_o 50 μm to 30 μm) is 1.52, 1.46, 1.44, and 1.44 times that of the Con-Coupler's maximum value over the entire frequency range. At f_2, the values are 1.68, 1.64, 1.66, 1.61, and 1.59 times. For L_a = 120 μm, at f_1, the values are 1.68, 1.53, 1.49, 1.39, and 1.39 times, and at f_2, they are 1.73, 1.66, 1.65, 1.60, and 1.57 times. When L_a = 100 μm, at f_1, the values are 1.70, 1.56, 1.44, 1.38, and 1.31 times, and at f_2, they are 1.60, 1.57, 1.55, 1.54, and 1.49 times.

These results show that the Meta-Coupler's electric field coupling at the transistor's gate channel is significantly improved compared to traditional Con-Coupler, often exceeding 1.5 times and reaching up to 1.73 times. This enables independent control of the meta-atom and coupled antenna, allowing flexible adjustment of resonance positions for dual or multiple resonances. The Fano resonance further enhances the coupling capability, addressing the trade-off between operating frequency and intensity in Con-Couplers.

The Meta-Coupler architecture provides remarkable enhancement in local coupling electric field strength, while also significantly improving the detector's bandwidth. Fig. 8(a) illustrates the electric field intensity as a function of frequency at a point of interest under the gate for a Meta-Coupler with R_o = 20 μm and L_a = 100 μm, compared to a Con-Coupler with L_a = 100 μm.

The red shaded area indicates the frequency range where the Meta-Coupler's coupling electric field exceeds the maximum value E_{Con_max} of the traditional Con-Coupler. The gray shaded area indicates the frequency range where the Meta-Coupler 's coupling electric field exceeds half the maximum value $E_{Con\_max}/2$ of the Con-Coupler. The red shaded area covers approximately 474 GHz to 746 GHz, indicating that within this 272 GHz bandwidth, the coupling electric field intensity of the new architecture surpasses the maximum value of the traditional Con-Coupler. This means that, using the maximum coupling field strength of traditional detectors as a baseline, the Meta-Coupler architecture can greatly enhance the detector's operational bandwidth. The gray area spans 270 GHz to 474 GHz and 746GHz to 972 GHz. Using the half-peak value of the maximum field strength E_{Con_max} of the Con-Coupler as the benchmark, the new architecture achieves a bandwidth enhancement covering 270 GHz to 972 GHz, totaling 702 GHz. Achieving such a wide bandwidth with a single traditional architecture transistor detector is almost impossible, making this a significant breakthrough. Fig. 8(b) and (c) present the results for L_a = 120 μm *and* 140 μm, respectively. In these instances, the new architecture also exhibits ultra-wideband characteristics, with the red and gray shaded areas covering most of the frequency range from 0 to 1000 GHz. Similarly, Fig. 8(d), (e), and (f) illustrate the electric field intensity at the point of interest under the gate of Meta-Coupler as a function of R_o for L_a = 100 μm, 120 μm, and 140 μm, respectively. It can be seen that when R_o is relatively small, corresponding to the upper part of the

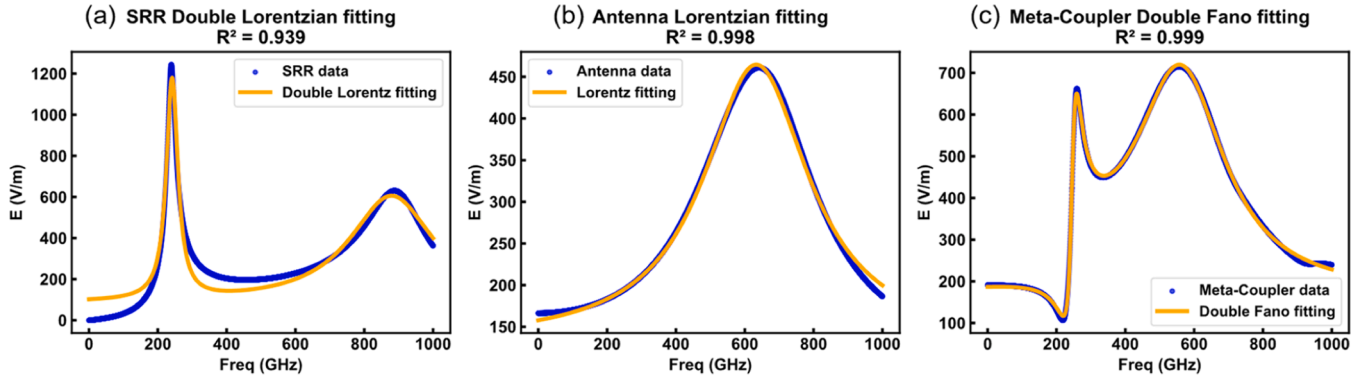

Fig. 7. (a) Double-Lorentzian fitting of the SRR, (b) single-Lorentzian fitting of the antenna, and (c) double-Fano fitting of the metasurface coupler.

Table 1
Lorentzian and Fano fitting results and related parameters for the near-field enhancement of the three devices.

Type	Device	Mode	$F_{resonant}$ (GHz)	Damping rate(GHz)	Q factor	Fano asymmetry parameter
Lorentzian	Antenna	Mode1	633.0	186.7	1.7	–
Double Lorentzian	SRR	Mode1	241.6	20.2	6.0	–
		Mode2	879.4	150.0	2.9	–
Double Fano	Meta-Coupler	Mode1	246.8	17.2	7.2	$q = 1.49$
		Mode2	565.5	158.2	1.8	$q = 0.04$

Table 2
Resonance points f_{Con} and their corresponding peak electric field strengths for Con-Couplers, and resonance points f_1, f_2 and their corresponding field strengths for Meta-Couplers, as shown in Fig. 6.

	Con-Coupler	Meta-Coupler				
R_o / L_a	0	50	45	40	35	30
140	$f_{Con1} = 476$ $E_{Con1\_max} = 668$	$f_1 = 211$ $E_1 = 1017$ $f_2 = 431$ $E_2 = 1125$	$f_1 = 234$ $E_1 = 972$ $f_2 = 432$ $E_2 = 1093$	$f_1 = 261$ $E_1 = 965$ $f_2 = 431$ $E_2 = 1107$	$f_1 = 295$ $E_1 = 945$ $f_2 = 432$ $E_2 = 1076$	$f_1 = 335$ $E_1 = 959$ $f_2 = 430$ $E_2 = 1060$
120	$f_{Con2} = 537$ $E_{Con2\_max} = 551$	$f_1 = 212$ $E_1 = 924$ $f_2 = 476$ $E_2 = 951$	$f_1 = 235$ $E_1 = 842$ $f_2 = 479$ $E_2 = 912$	$f_1 = 261$ $E_1 = 821$ $f_2 = 481$ $E_2 = 911$	$f_1 = 293$ $E_1 = 764$ $f_2 = 481$ $E_2 = 882$	$f_1 = 336$ $E_1 = 766$ $f_2 = 480$ $E_2 = 867$
100	$f_{Con3} = 641$ $E_{Con3\_max} = 461$	$f_1 = 212$ $E_1 = 785$ $f_2 = 520$ $E_2 = 739$	$f_1 = 234$ $E_1 = 717$ $f_2 = 543$ $E_2 = 725$	$f_1 = 259$ $E_1 = 662$ $f_2 = 557$ $E_2 = 716$	$f_1 = 294$ $E_1 = 637$ $f_2 = 558$ $E_2 = 708$	$f_1 = 337$ $E_1 = 603$ $f_2 = 558$ $E_2 = 685$

graphs, the Fano resonance peaks introduced by the meta-atom and the bowtie-antenna are very close in position, resulting in their overlap and forming a broader main peak. However, as R_o increases, corresponding to the lower part of the image, the position difference between the two resonance peaks widens, and the resonance peak introduced by R_o gradually separates from the main peak. In contrast, the resonance peak of the bowtie-antenna remains almost unchanged, appearing as a nearly vertical line parallel to the $y-axis$. This phenomenon is further evidenced by the red dashed line, which clearly bifurcates with increasing R_o. This observation provides additional support for the theoretical analysis of the two resonance modes in the Meta-Coupler architecture, specifically the adjustable resonance introduced by the meta-atom and the resonance peak from the bowtie-antenna. Additionally, as the position difference between the two resonance peaks increases, small regions between $200-400$ GHz in Fig. 8(d), (e), and (f) show electric field intensities that do not exceed E_{Con_max} (but still exceed the half-peak height). This is due to the separation of the two resonance peaks, resulting in a diminished enhancement effect in the middle frequency range. Additionally, Fig. 8(d) demonstrates that as R_o increases, the bandwidth enhancement effect of the new architecture is further amplified, with the frequency range covered by the two black dashed lines expanding. The horizontal width of these black dashed lines is positively correlated with R_o, indicating that for $L_a = 100$ μm, adjusting R_o can increase the Meta-Coupler's bandwidth beyond 702 GHz. This phenomenon is similarly observed in Fig. 8(e) and (f). The Meta-Coupler architecture leverages Fano resonance introduced by meta-atoms, leading to a dramatic improvement in detector bandwidth. Our analysis shows that the structure of the meta-atom significantly influences the detector's bandwidth. Subsequent efforts can concentrate on developing multi-frequency resonant meta-atoms to achieve full-band enhancement.

Additionally, for the case of $L_a = 100$ μm and $R_o = 50$ μm, a polar-

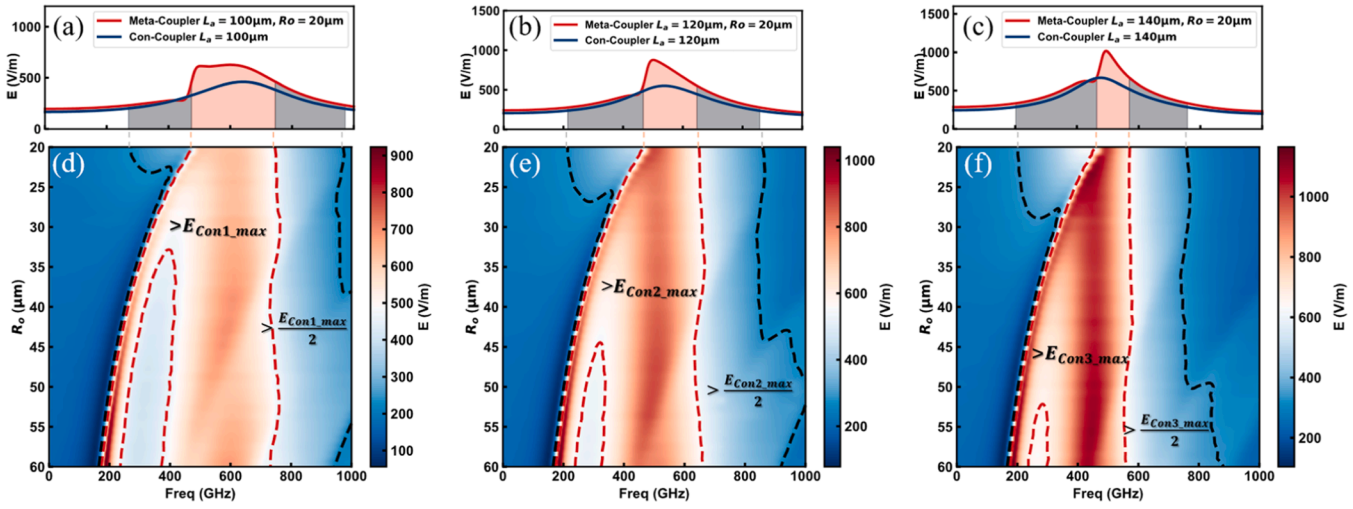

Fig. 8. (a), (b), and (c) depict the curves of electric field intensity as a function of frequency for Meta-Coupler with $R_o = 20$ μm and $L_a = 100,\ 120,$ and 140 μm, respectively, in comparison to Con-Coupler of the same length L_a. The red shaded area indicates the frequency range where the electric field intensity exceeds the maximum value of the Con-Coupler, while the gray shaded area indicates the frequency range where the intensity exceeds half the maximum value of the Con-Coupler. Similarly, (d), (e), and (f) present the electric field intensity at points of interest under the gate of Meta-Coupler as a function of R_o for $L_a = 100$ μm, 120 μm and 140 μm, respectively.

ization angle analysis was conducted on the near-field enhancement at the center of the gated channel across multiple frequencies. As shown in Fig. 9, at the SRR-induced resonance frequency of 261 GHz, a characteristic linear polarization reception scenario is observed, where a polarization angle of 0° yields the strongest near-field electric field enhancement. Similarly, in Fig. 9(b) and (c), which examine the higher-frequency region dominated primarily by the bowtie antenna, maximum near-field enhancement is also achieved under standard linear polarization. However, due to the mutual interference between the SRR and the bowtie structure, the optimal reception angle is no longer 0° Nevertheless, in this study, a polarization angle of 0° is adopted, as it more closely aligns with practical conditions.

3.3. Resonant frequency prediction for meta-couplers by KAN deep learning

The novel Meta-Coupler architecture leverages Fano resonance enhancement to introduce a new mechanism into HEMT-based detectors. While this advancement improves performance, it also brings about certain challenges. As demonstrated in Table 1, a comparison of the resonance frequencies f_1 and f_2 of Meta-Coupler with the resonance frequency f_{Con} of Con-Coupler, along with the resonance frequency data of the meta-atom shown in Fig. 4, indicates that the Fano resonance causes the two resonance peaks, f_1 and f_2, of the new Meta-Coupler architecture to diverge from a simple linear combination of the meta-atom's resonance peak and the Con-Coupler's resonance peak. For instance, when the parameter L_a decreases from 140 μm to 100 μm, the f_2 resonance peak of the Meta-Coupler, associated with the bowtie antenna, shifts relative to the Con-Coupler resonance peak by 9.7 %, 11.4 %, and 18.9 %. This shift becomes more pronounced as L_a further decreases. A similar trend is observed for the f_1 resonance peak associated with the meta-atom. Consequently, predicting the exact resonance peaks f_1 and f_2 for specific Meta-Coupler structural parameters is highly challenging. This difficulty arises from the nonlinear coupling between the meta-atom and the bowtie antenna, leading to Fano resonance. As a result, it is not feasible to simply predict f_1 and f_2 through a linear combination of the existing resonance data of the meta-atom and the bowtie antenna. To address this issue, the use of a forward prediction model based on KAN has been pioneered in the field of THz detectors.

KAN is a novel neural network architecture proposed in [37], which we have successfully applied to this study. Unlike Multi-Layer-Perception (MLP), KAN performs nonlinear transformations and feature extraction based on the Kolmogorov-Arnold representation theorem. It exhibits excellent performance in solving partial differential equations, dynamical modeling, and physical model simulation. Kolmogorov-Arnold Representation Theorem states that any multidimensional continuous function defined over a bounded domain can be represented as a finite sum of continuous functions of a single variable. Specifically, an n-dimensional continuous function $f(x_1, x_2, \ldots, x_n)$ can be represented as:

$$f(\mathbf{x}) = \sum_{i=1}^{2n+1} \Phi_i \left(\sum_{j=1}^{n} \phi_{i,j}(x_j) \right) \tag{8}$$

Based on this theorem, each KAN layer consists of two neural network layers, where $\phi_{i,j}$ and Φ_i are single-variable continuous functions corresponding to the neurons of the first and second layer respectively. The first layer of the KAN layer is edge function layer, which nonlinearly transforms the input data and passes the transformed results to the next layer. The edge functions are represented using spline functions (B-splines):

$$\phi_{i,j}(x) = \sum_{k=k_{i,j}}^{k_{i,j}+r_{i,j}} c_{i,j,k} B_k(x) \tag{9}$$

Where $B_k(x)$ represents the basis functions of B-splines, $c_{i,j,k}$ are the learned parameters, $k_{i,j}$ and $r_{i,j}$ are the starting index and order of the spline functions, respectively. In KAN training, the spline parameters $c_{i,j,k}$ of the edge functions are optimized. These parameters control the shape of the edge functions and the degree of nonlinear transformation. The second layer is the node layer, which computes a weighted sum of the outputs from all edge functions in the first layer:

$$\Phi_i = \sum_{j=1}^{m_i} \phi_{i,j}(x_j) \tag{10}$$

Here, Φ_i represents the output of the node layer, which is the output of this KAN layer. Unlike traditional MLPs, the node layer in KAN does

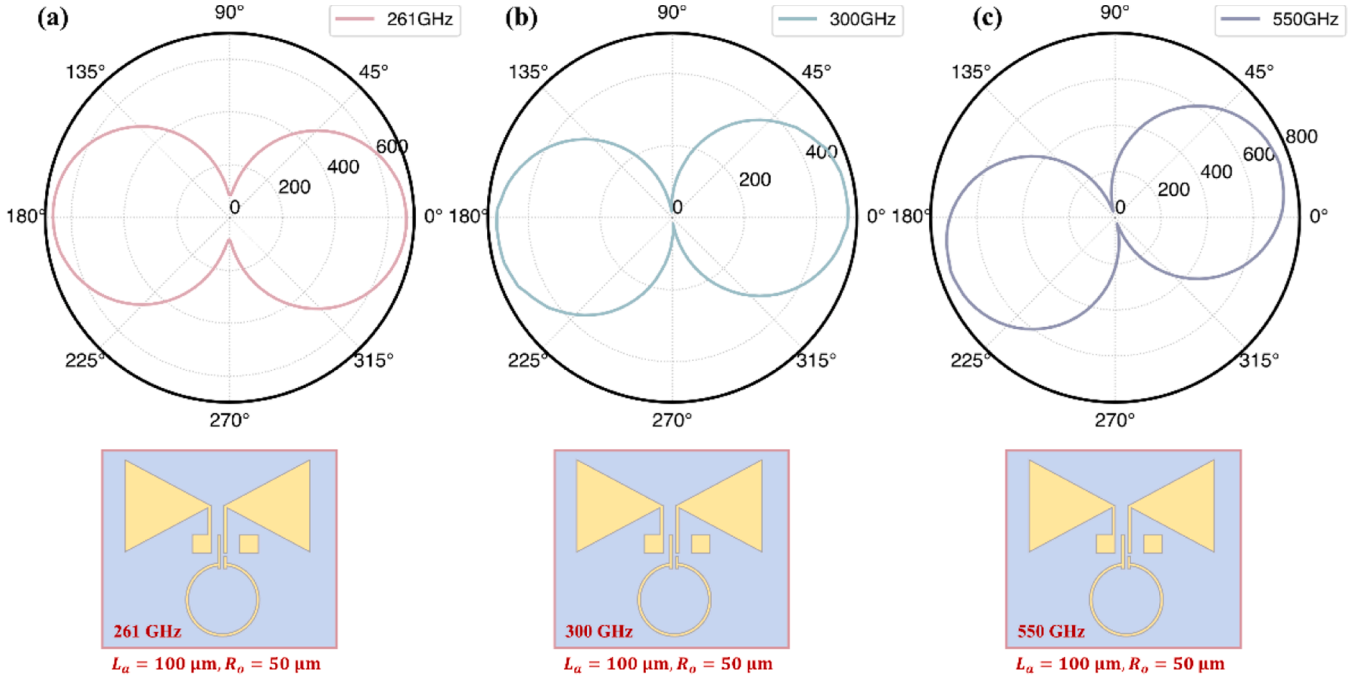

Fig. 9. Sensitivity analysis of near-field enhancement with respect to polarization angle: (a) 261 GHz, (b) 300 GHz, (c) 550 GHz.

not apply nonlinear activation functions. Instead, it simply performs a linear combination of the outputs of all edge functions to accurately represent complex function relationships.

KAN decompose complex multivariate functions into finite combinations of single-variable functions, thereby simplifying the representation and learning process of complex functions. Compared to MLPs, KANs are more effective at representing the nonlinear relationships in complex functions and possess better model interpretability and parameter efficiency. In this study, we utilized KAN layers to learn the mapping function from the key parameters R_o and L_a to the electric field intensity. As shown in Fig. 10(a), we have developed a multi-layer KAN network has been developed. It takes R_o and L_a as inputs and outputs the electric field intensity magnitudes at 3012 discrete frequency points within the $0-1000$ GHz range. This KAN network enables the prediction of the electric field intensity curve with high precision, providing detailed insights into the relationship between the input parameters and the resulting field intensities.

Datasets We simulated 246 electric field intensity curves using CST software. In these curves, the R_o ranged from 20 to 60 with a step size of 1, and L_a ranged from 100 to 150 with a step size of 10. We randomly and evenly selected 171 cases of the training set to train the KAN algorithm, 38 cases of the evaluation set to optimize model parameters, and 37 cases of the test set for testing algorithm performance.

Training The KAN algorithm was implemented in Python using PyTorch, utilizing a NVIDIA GeForce GTX 3060 GPU. It was trained using the Adam optimizer with a weight decay of 10–3. The initial learning rate was set to 10–3, and a batch size of 64 was used. The loss function employed was Mean Squared Error (MSE). The maximum number of epochs was set to 30,000, and the model that performed best on the validation set was selected as the final model.

Experiment We evaluated the influence of different numbers of KAN layers on model performance. Specifically, we used 1, 2, 4, and 8 layers of KAN layers for predicting electric field intensity. For each additional KAN layer, the number of input and output channels was set to 128. Fig. 10(b) illustrates the evolution of the loss function for networks with varying numbers of layers over 5000 epochs. It is evident that networks with more layers show faster rates of loss reduction. Moreover, models with more layers achieve lower loss within the same number of training epochs. Fig. 10(c) shows the performance of models with varying numbers of layers on the validation set. It can be observed that as the number of layers increases, the network achieves progressively lower loss, with the 8-layer network exhibiting the best performance as our

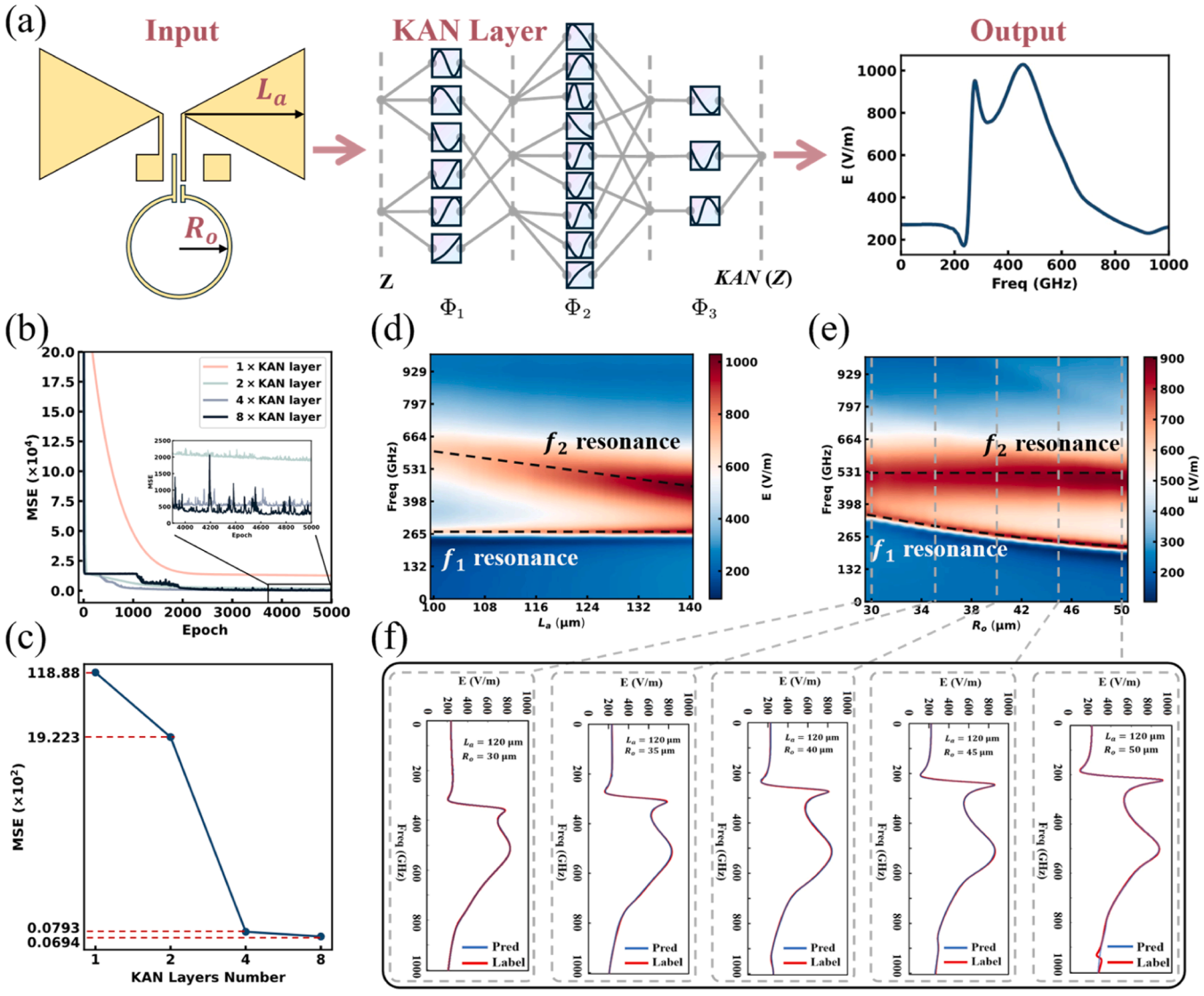

Fig. 10. (a) Schematic diagram of the KAN based coupled electric field prediction network (b) Evolution of loss functions in coupled electric field prediction networks with different KAN Layer depths (c) MSE for KAN with varying numbers of layers (d) Predicted distribution of electric field intensity as L_a varies when $R_o = 40$ μm (e) Predicted distribution of electric field intensity as R_o varies when $L_a = 120$ μm (f) Comparison of predicted and actual values for five Meta-Couplers.

final model for predicting electric field intensity. This experiment confirms that the deeper KAN networks show the stronger learning capability for the physical model studied in our research. However, as the number of network layers increases, the rate of improvement in algorithm performance decreases.

The performance of the deep KAN network was evaluated using the test set. The MSE for the electric field estimation was 38.68, with an average runtime of 7.8 ms for one case. In the test set, the electric field intensity varies from 0 to 1300. Our method achieves an average absolute error of 3.96±1.69 V/m for predicting the electric field intensity curve. The examples of predicted electric field intensity are shown in Fig. 10(d) and (f). Our network predictions perfectly align with the trends analyzed in Fig. 6. Specifically, when R_o is fixed, varying L_a impacts only the resonance point f_2, while the resonance point f_1, determined by SRR, remains almost constant. Conversely, when L_a is fixed, the network's predictions match the known results, showing that f_2 remains unchanged while f_1 shifts to a lower frequency as ro increases. Notably, for the critical cases of $L_a = 120$ μm and R_o values of 30, 35,

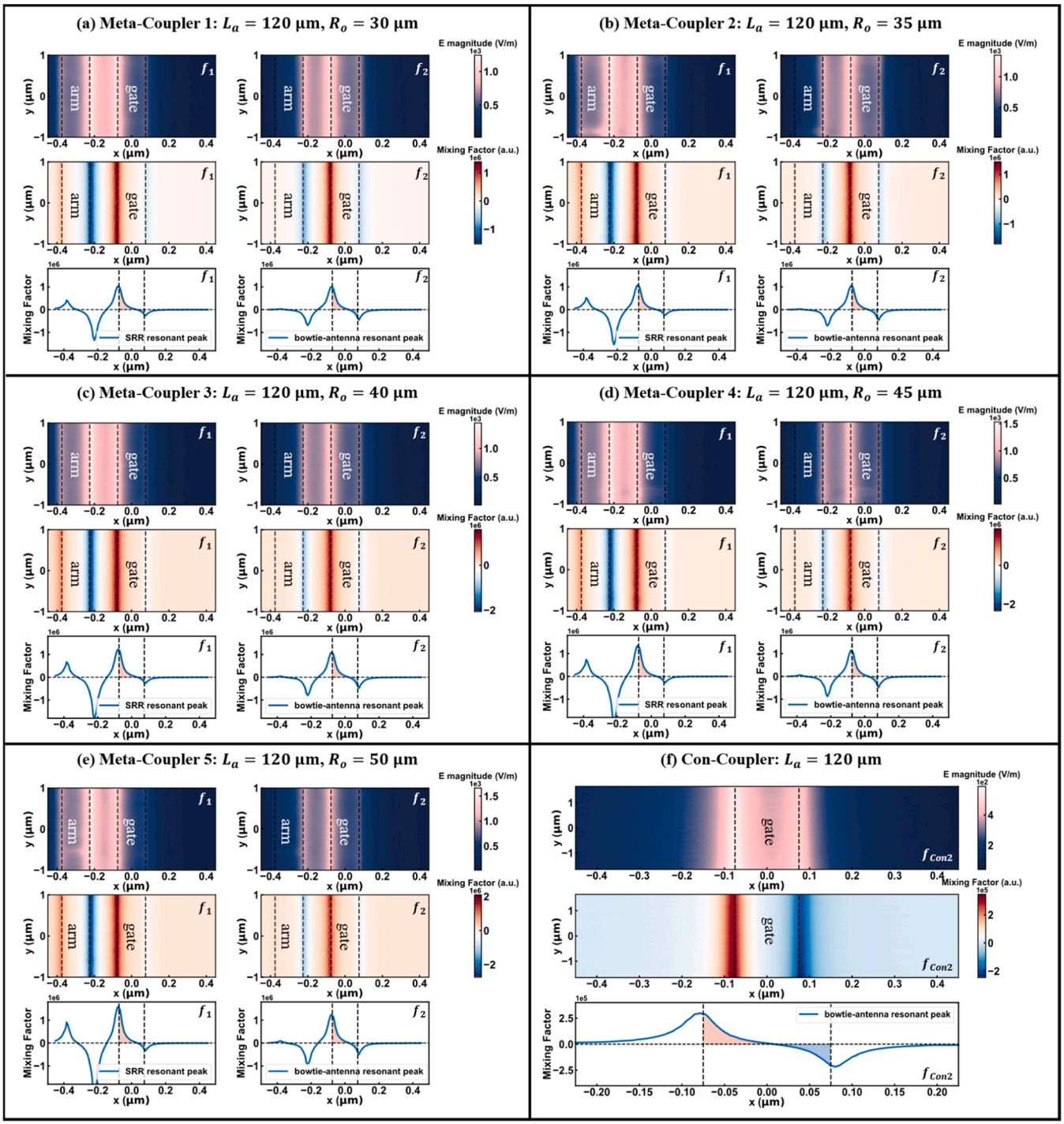

Fig. 11. Electric field and mixing factor distributions in the channel plane for (a)-(e) five Meta-Couplers with $L_a = 120$ μm and $R_o = 30, 35, 40, 45, 50$ μm, shown at Fano resonances f_1 and f_2. (f) Con-Coupler ($L_a = 120$ μm) distributions at its resonance frequency. Dashed lines indicate gate boundaries. $M(x)$ curves show opposite-direction self-mixing currents (pink and blue shading) with peak values at gate edges, demonstrating the distinct double phase reversal in Meta-Couplers versus single reversal in Con-Coupler.

40, 45, and 50 μm, our model accurately predicts the positions of the resonance peaks f_1 and f_2. The KAN-based electric field intensity prediction network developed can rapidly and accurately predict the electric field intensity curve in response to given parameters R_o and L_a. Moreover, it can provide a more continuous and precise trend of electric field intensity variations within the given parameter range.

3.4. Comparing the antenna factor performance: meta-coupler vs. con-coupler

According to the self-mixing model of field-effect transistors at zero source-drain bias (Eq. (2)), the photocurrent is primarily determined by the antenna factor $\Lambda_0(\omega) = \int_0^L \dot{\xi}_x \dot{\xi}_z \cos\phi \mathrm{d}x$, which quantifies the terahertz field coupling capability, and the field-effect factor $\Xi(V_g)$, which represents the gate control capability. The mixing factor in Eq. (1), derived from decomposing the antenna factor, effectively illustrates the self-mixing phenomenon within the gate-controlled channel layer. All terahertz fields ($\dot{\xi}_x$ and $\dot{\xi}_z$) are normalized to the incident field intensity E_0.

To systematically compare the performance, we selected five Meta-Couplers validated by our KAN-based prediction network (Fig. 11(f)) and one conventional Con-Coupler, all with identical antenna length $L_a = 120$ μm. The Meta-Couplers feature meta-atom radii of 30, 35, 40, 45, and 50 μm to investigate the impact of meta-atom size. All field data in Fig. 11 represent the in-plane distribution within the 2DEG channel, located 23 nm beneath the metal gate, with gate and arm regions marked by gray dashed lines.

Fig. 11 presents the field distributions for Meta-Couplers at frequencies f_1 and f_2, and for Con-Coupler at f_{Con1}, with specific frequencies listed in Table 1. Each row displays the in-plane electric field intensity, mixing factor distribution, and the y-averaged $M(x)$ curve. For the Con-Coupler at $f_{Con1} =$ 537 GHz (Fig. 11(f)), the electric field intensity strongly localizes at the gate edges, particularly on the source side due to asymmetric antenna coupling. The mixing factor distribution exhibits similar asymmetry, generating opposite-sign factors near the source ($-x$) and drain ($+x$) sides. The $M(x)$ curve reveals stronger mixing on the source side compared to the drain side, with extrema at gate edges. Although the π phase flip creates opposing currents, intensity differences yield a net unidirectional mixing current. Integration over the gate-controlled region yields an antenna factor of 3105,719, serving as our performance baseline.

The Meta-Coupler demonstrates fundamentally different field characteristics. In Meta-Coupler1 (Fig. 11(a)), high-intensity fields concentrate between the arm and gate, specifically at the arm's right boundary and gate's left boundary—a stark contrast to the Con-Coupler's gate-centered distribution. Remarkably, the $M(x)$ curve exhibits double phase reversal within the specified range, occurring under both the gate and meta-atom arm, compared to the single reversal in conventional designs. This distinctive behavior manifests in two resonance modes with different physical origins.

At the f_1 frequency (first column), the mixing factor at the arm's right edge dramatically exceeds that at the gate's right edge, with pronounced reversals within the gap region. This behavior, attributed to Fano resonance arising from the coupling between the SRR and bow-tie antenna, dominates the terahertz field enhancement. Conversely, at the f_2 frequency (second column), the mixing factor intensity at the arm boundary significantly diminishes, with comparable $M(x)$ values at arm and gate edges. The nearly vanishing positive mixing factor on the arm's left side indicates minimal meta-atom contribution, with enhancement primarily from the coupled antenna resonance.

The mixing intensity correlation with meta-atom radius R_o proves particularly significant. As demonstrated from Fig. 11(a) to 10(e), increasing R_o produces more pronounced $M(x)$ peaks, substantially enhancing mixing efficiency—consistent with observations in Fig. 4(a). Since only the gate-controlled region participates in self-mixing (where the field-effect factor $\Xi(V_g) = dG/dVg$ varies significantly), we integrated $M(x)$ exclusively over this region to obtain antenna factors.

The performance comparison yields remarkable results. At the Fano resonance frequency f_1, the antenna factors are: Meta-Coupler1: 24,620,297 (25.2× enhancement); Meta-Coupler2: 26,231,037 (33.7× enhancement); Meta-Coupler3: 30,856,545 (45.5× enhancement); Meta-Coupler4: 33,895,783 (55.1× enhancement); and Meta-Coupler5: 40,015,076 (69.7× enhancement). At the antenna resonance frequency f_2, enhancement factors range from 7.8× to 10.4×. Fig. 12 visualizes these comparisons, with green representing conventional detectors and red representing Meta-Couplers.

These results demonstrate two transformative advances for terahertz field-effect detectors. First, across the entire 0–1000 GHz band, the Meta-Coupler achieves unprecedented sensitivity enhancement, reaching 69.7-fold improvement at the Fano resonance point. This confirms that our devices exploit electrostatic control of collective electromagnetic interactions at deep subwavelength scales [38], enabling applications in trace chemical spectroscopy [39]and room-temperature terahertz medical imaging [40]. Second, the working bandwidth is dramatically expanded—a single Meta-Coupler ($L_a = 100$ μm, $R_o = 20$ μm) achieves 702 GHz bandwidth (270–972 GHz), an ultra-wideband capability fundamentally unattainable with conventional architectures. These achievements establish the Meta-Coupler as a paradigm shift in terahertz detection technology.

4. Conclusion

This study proposes a novel Meta-Coupler architecture and an associated deep-learning prediction framework. To the best of current knowledge, this work represents the first systematic quantitative study introducing a Fano resonance-enhanced meta-array into HEMT-based terahertz detection. Additionally, the introduction of a KAN-based deep-learning method significantly advances the rapid and accurate prediction of coupling-induced Fano resonances within field-effect detection systems.

The designed Meta-Array, composed of high-Q meta-atoms, generates pronounced Fano resonances when integrated with on-chip antennas, offering a new mechanism for sensitivity enhancement. This enhancement substantially improves detector sensitivity to terahertz radiation and facilitates flexible tuning of highly responsive frequency bands to satisfy diverse application requirements. Performance analysis of a strongly coupled split-ring resonator combined with a GaN HEMT-based detector within the frequency range of 270–972 GHz demonstrates a remarkable sensitivity improvement of approximately 70-fold at specific resonance frequencies, along with significantly enhanced coupling efficiency throughout nearly the entire measurement spectrum. These findings confirm that integrating high-Q meta-arrays with GaN HEMTs to leverage Fano resonance provides an effective solution for achieving ultra-sensitive, room-temperature detection and spectral analysis in the millimeter-wave and terahertz frequency bands. The proposed Meta-Coupler architecture and KAN-based prediction network exhibit versatility and are readily adaptable to other HEMT-based THz detector technologies.

CRediT authorship contribution statement

Yihao Li: Project administration, Methodology, Investigation. **Yuxuan Zhai:** Project administration, Methodology, Investigation, Visualization. **Jiandong Sun:** Resources, Methodology, Investigation. **Shengji Wang:** Project administration, Methodology. **Haoran Wang:** Formal analysis, Data curation. **Xiaojiao Deng:** Formal analysis, Data curation. **Xinhua Li:** Investigation, Funding acquisition, Formal analysis. **Shijie Wang:** Formal analysis, Data curation. **Chengkuo Lee:** Supervision,

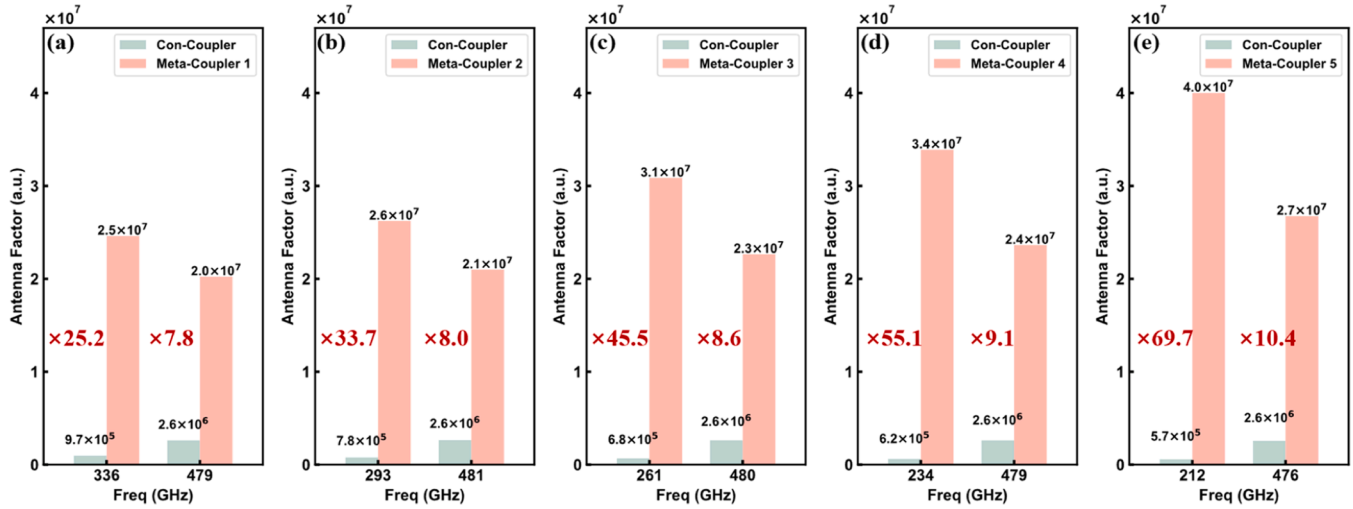

Fig. 12. Comparison of the antenna factors at two representative resonance frequencies for Meta-Coupler 1–5 and the traditional Con-Coupler. The Meta-Couplers exhibit performance that is several times higher than that of the traditional Con-Coupler.

Software, Data curation. **Xiaoping Zheng:** Funding acquisition, Formal analysis, Conceptualization.

Declaration of competing interest

The authors declare that they have no competing interests.

Funding

This research was supported by the Key Technologies Research and Development Program (2023YFB3207800); National Natural Science Foundation of China (61927804).

Acknowledgement

The authors acknowledge the support of the Tsinghua University Cloud Computing Platform for providing computational resources during the modeling and simulation process. The authors also sincerely thank Prof. Qin Hua from the Suzhou Institute of Nano-Tech and Nano-Bionics for valuable guidance on the development of the detector modeling.

Data availability

Data will be made available on request.

References

[1] Yang X, Zhao X, Yang K, Liu Y, Liu Y, Fu W, Luo Y. Biomedical applications of terahertz spectroscopy and imaging. Trends Biotechnol 2016;34:810–24.
[2] Zhang Z, Zhong C, Fan F, Liu G, Chang S. Terahertz polarization and chirality sensing for amino acid solution based on chiral metasurface sensor. Sens Actuators B Chem 2021;330:129315.
[3] Lyu J, Huang L, Chen L, Zhu Y, Zhuang S. Review on the terahertz metasensor: from featureless refractive index sensing to molecular identification. Photonics Res 2024;12:194–217.
[4] Wang Y, Fan F, Zhao H, Ji Y, Liu J, Chang S. Terahertz active multi-channel vortices with parity symmetry breaking and near/far field multiplexing based on a dielectric-liquid crystal-plasmonic metadevice‘. Opto-Electron Adv 2025;8. 240250-1-240250–12.
[5] Zhao H, Guo J, Fan F, Wang Y, Liu J, Wang H, Li F, Ji Y, Cheng J, Chang S. Active broadband terahertz OAM-based metalens based on multi-channel multiplexing. Laser Photonics Rev 2025:2402084.
[6] Zhao H, Fan F, Wang Y, Liu J, Ji Y, Cheng J, Chang S. Vortex-vector beam conversion and chiral field manipulation based on terahertz liquid crystal cascaded metadevice. Laser Photonics Rev 2024;18:2400442.
[7] Hawecker J, Pistore V, Minasyan A, Maussang K, Palomo J, Sagnes I, Manceau J-M, Colombelli R, Tignon J, Mangeney J, Dhillon SS. Cavity-based photoconductive sources for real-time terahertz imaging. Photonics Res 2020;8:858–63.
[8] Stantchev RI, Sun B, Hornett SM, Hobson PA, Gibson GM, Padgett MJ, Hendry E. Noninvasive, near-field terahertz imaging of hidden objects using a single-pixel detector. Sci Adv 2016;2:e1600190.
[9] Liu B, Peng Y, Hao Y, Zhu Y, Chang S, Zhuang S. Ultra-wideband terahertz fingerprint enhancement sensing and inversion model supported by single-pixel reconfigurable graphene metasurface. PhotoniX 2024;5:10.
[10] Han W, Wang P, Zhang C, Xu Y, Wu Z, Wang Q. Pixelated toroidal metasurface sensor with broadband terahertz fingerprint enhancement for biochemical trace detection. ACS Appl Mater Interfaces 2024.
[11] Xie Y, Ma Y, Liu X, Khan SA, Chen W, Zhu L, Zhu J, Liu QH. Dual-degree-of-freedom multiplexed metasensor based on quasi-BICs for boosting broadband trace isomer detection by THz Molecular fingerprint. IEEE J Sel Top Quantum Electron 2023;29:1–10.
[12] Delfanazari K, Klemm RA, Joyce HJ, Ritchie DA, Kadowaki K. Integrated, portable, tunable, and coherent terahertz sources and sensitive detectors based on layered superconductors. Proc IEEE 2020;108:721–34.
[13] Rasekh P, Safari A, Yildirim M, Bhardwaj R, Ménard J-M, Dolgaleva K, Boyd RW. Terahertz nonlinear spectroscopy of water vapor. ACS Photonics 2021;8:1683–8.
[14] Li Y, Sun J, Qin C, Deng X, Zheng X. A high-performance terahertz detector based on a graded channel GaN high-electron-mobility transistor with a recessed gate. Opt Mater 2024;150:115233.
[15] Tamura K, Tang C, Ogiura D, Suwa K, Fukidome H, Takida Y, Minamide H, Suemitsu T, Otsuji T, Satou A. Fast and sensitive terahertz detection with a current-driven epitaxial-graphene asymmetric dual-grating-gate field-effect transistor structure. APL Photonics 2022;7:126101.
[16] Zhu Y, Ding Q, Xiang L, Zhang J, Li X, Jin L, Shangguan Y, Sun J, Qin H. 0.2-4.0 THz broadband terahertz detector based on antenna-coupled AlGaN/GaN HEMTs arrayed in a bow-tie pattern. Opt Express 2023;31.
[17] Zhu K, Feng W, Zhu Y, Ding Q, Wang Y, Xiao Y, Jin L, Qin H, Sun H. Waveguide-coupled heterodyne terahertz detector based on AlGaN/GaN high-electron-mobility transistor. Appl Phys Lett 2022;121:081101.
[18] Feng W, Zhu Y, Ding Q, Zhu K, Sun J, Zhang J, Li X, Shangguan Y, Jin L, Qin H. Heterodyne terahertz detection based on antenna-coupled AlGaN/GaN high-electron-mobility transistor. Appl Phys Lett 2022;120.
[19] Sun J, Feng W, Ding Q, Zhu Y, Zhang Z, Li X, Qin H, Zhang J, Li X, Yang S, Jin L, Sun Y, Popov VV. Smaller antenna-gate gap for higher sensitivity of GaN/AlGaN HEMT terahertz detectors. Appl Phys Lett 2020;116.
[20] Sun J, Zhu Y, Feng W, Ding Q, Qin H, Sun Y, Zhang Z, Li X, Zhang J, Li X, Shangguan Y, Jin L. Passive terahertz imaging detectors based on antenna-coupled high-electron-mobility transistors. Opt Express 2020;28:4911–20.
[21] Sun J, Zhang Z, Li X, Qin H, Sun Y, Cai Y, Yu G, Zhang Z, Zhang J, Shangguan Y, Jin L, Li X, Zhang B, Popov VV. Two-terminal terahertz detectors based on AlGaN/GaN high-electron-mobility transistors. Appl Phys Lett 2019;115.
[22] Huang R, Ji X, Liao Y, Peng J, Wang K, Xu Y, Yan F. Dual-frequency CMOS terahertz detector with silicon-based plasmonic antenna. Opt Express 2019;27: 23250–61.
[23] Huang Z, Yan W, Li Z, Dong H, Yang F, Wang X. High-responsivity, low-leakage current, ultra-fast terahertz detectors based on a GaN High-electron-mobility transistor with integrated bowtie antennas. Sensors 2022;22:933.
[24] Satou A, Negoro T, Narita K, Hosotani T, Tamura K, Tang C, Lin T-T, Retaux P-E, Takida Y, Minamide H, Suemitsu T, Otsuji T. Gate-readout and a 3D rectification effect for giant responsivity enhancement of asymmetric dual-grating-gate plasmonic terahertz detectors. Nanophotonics 2023;12:4283–95.
[25] Bauer M, Rämer A, Chevtchenko SA, Osipov KY, Čibiraitė D, Pralgauskaitė S, Ikamas K, Lisauskas A, Heinrich W, Krozer V, Roskos HG. A high-sensitivity AlGaN/GaN HEMT terahertz detector with integrated broadband bow-tie antenna. IEEE Trans Terahertz Sci Technol 2019;9:430–44.

[26] Attiaoui A, Daligou G, Assali S, Skibitzki O, Schroeder T, Moutanabbir O. Polarization-tuned fano resonances in all-dielectric short-wave infrared metasurface. Adv Mater 2023;35:2300595.
[27] Limonov MF, Rybin MV, Poddubny AN, Kivshar YS. Fano resonances in photonics. Nat Photonics 2017;11:543–54.
[28] Melik-Gaykazyan E, Koshelev K, Choi J-H, Kruk SS, Bogdanov A, Park H-G, Kivshar Y. From fano to quasi-BIC resonances in individual dielectric nanoantennas. Nano Lett 2021;21:1765–71.
[29] Li Y, Chen R, Sun J, Deng X, Li X, Xie Y, Wang S, You Z, Qin C, Zheng X. Deep-learning-driven design of multiplexed meta-array couplers for broadband HEMT terahertz detection. Photonics Res 2025;13:1290–301.
[30] Dong T, Li S, Manjappa M, Yang P, Zhou J, Kong D, Quan B, Chen X, Ouyang C, Dai F, Han J, Ouyang C, Zhang X, Li J, Li Y, Miao J, Li Y, Wang L, Singh R, Zhang W, Wu X. Nonlinear THz-nano metasurfaces. Adv Funct Mater 2021;31:2100463.
[31] Qin H, Sun J, Liang S, Li X, Yang X, He Z, Yu C, Feng Z. Room-temperature, low-impedance and high-sensitivity terahertz direct detector based on bilayer graphene field-effect transistor. Carbon N Y 2017;116:760–5.
[32] Chernyadiev AV, But DB, Ivonyak Y, Ikamas K, Lisauskas A. A CMOS-integrated terahertz near-field sensor based on an ultra-strongly coupled meta-atom. Sci Rep 2024;14:11483.
[33] Zhao Y, Wang L, Zhang Y, Qiao S, Liang S, Zhou T, Zhang X, Guo X, Feng Z, Lan F, Chen Z, Yang X, Yang Z. High-speed efficient terahertz modulation based on tunable collective-individual State conversion within an active 3 nm two-dimensional electron gas metasurface. Nano Lett 2019;19:7588–97.
[34] Yang Y, Kravchenko II, Briggs DP, Valentine J. All-dielectric metasurface analogue of electromagnetically induced transparency. Nat Commun 2014;5:5753.
[35] Khanikaev AB, Wu C, Shvets G. Fano-resonant metamaterials and their applications. Nanophotonics 2013;2:247–64.
[36] Shen P, Ji Y, Yue X, Li Y, Han M, Ma Y, Meng M, Fan F, Chang S. Ultrasensitive terahertz microfluidic biosensor integrated with tetrahedral DNA nanostructure for specific detection of live cancer cells. Sens Actuators B Chem 2025;428:137252.
[37] Z. Liu, Y. Wang, S. Vaidya, F. Ruehle, J. Halverson, M. Soljačić, T.Y. Hou, and M. Tegmark, "KAN: kolmogorov-Arnold Networks," (2024).
[38] Samizadeh Nikoo M, Matioli E. Electronic metadevices for terahertz applications. Nature 2023;614:451–5.
[39] Swearer DF, Gottheim S, Simmons JG, Phillips DJ, Kale MJ, McClain MJ, Christopher P, Halas NJ, Everitt HO. Monitoring chemical reactions with terahertz rotational spectroscopy. ACS Photonics 2018;5:3097–106.
[40] Yan Z, Zhu L-G, Meng K, Huang W, Shi Q. THz medical imaging: from in vitro to in vivo. Trends Biotechnol 2022;40:816–30.